

Quadrupole collectivity beyond $N = 50$ in neutron-rich Se and Kr isotopes

B. Elman,^{1,2} A. Gade,^{1,2} D. Weisshaar,¹ D. Barofsky,^{3,*} D. Bazin,¹ P. C. Bender,¹ M. Bowry,^{1,†} M. Hjorth-Jensen,^{1,2,4}
K. W. Kemper,⁵ S. Lipschutz,^{1,2} E. Lunderberg,^{1,2} N. Sachmpazidi,³ N. Terpstra,³ W. B. Walters,⁶ A. Westerberg,³
S. J. Williams,^{1,‡} and K. Wimmer^{1,3,§}

¹National Superconducting Cyclotron Laboratory, Michigan State University, East Lansing, Michigan 48824, USA

²Department of Physics and Astronomy, Michigan State University, East Lansing, Michigan 48824, USA

³Department of Physics, Central Michigan University, Mount Pleasant, Michigan 48859, USA

⁴Department of Physics and Center of Mathematics for Applications, University of Oslo, N-0316 Oslo, Norway

⁵Department of Physics, Florida State University, Tallahassee, Florida 32306, USA

⁶Department of Chemistry, University of Maryland, College Park, Maryland 20742, USA

(Received 7 July 2017; published 27 October 2017)

We report $B(E2; 0_1^+ \rightarrow 2_1^+)$ strengths for the neutron-rich $^{88,90}\text{Kr}$ and ^{86}Se isotopes from intermediate-energy Coulomb excitation. The electric quadrupole transition strengths to the first 2^+ states complete, with considerably improved uncertainties, the evolution of quadrupole collectivity in the Kr and Se isotopes approaching $N = 60$, for which ^{90}Kr and ^{86}Se had previously been the most uncertain. We also report significant excitation strength to several higher-lying 2^+ states in the krypton isotopes. This fragmentation of $B(E2)$ strength in $^{88,90}\text{Kr}$ confirms shell-model calculations in the $\pi(fpg)\text{-}\nu(sdgh)$ shell with an only minimally tuned shell-model setup that is based on a nucleon-nucleon interaction derived from effective field theory and effective charges adjusted to ^{86}Kr .

DOI: 10.1103/PhysRevC.96.044332

I. INTRODUCTION

The neutron-rich Zr, Sr, Kr, and Se isotopes with neutron numbers $N = 50\text{--}60$ continue to attract attention for their display of rapid changes in the evolution of collectivity and the mounting evidence for shape coexistence. Since the first indications from the trends in the first 2^+ energies in Zr [1] and Sr [2] decades ago, studies of transition strengths and moments have most recently cemented a picture of a sudden increase in collectivity and shape changes for Sr [3–6] and a quantum phase transition in the shape of the Zr isotopes [7–9] at $N = 60$.

In the Kr isotopic chain, just four and two protons below Zr and Sr, respectively, a rather gradual onset of collectivity towards $N = 60$ was concluded from mass measurements [10], Coulomb excitation [11], and fast-timing measurements [12], placing the $N = 60$ isotone ^{96}Kr at the low- Z boundary of the region of deformation described above [13].

Comparably little is known about the evolution of collectivity in the Se isotopes. Information is limited to excitation energies out to ^{94}Se [14–16], the $B(E2 \uparrow)$ strength of ^{84}Se from Coulomb excitation [17], and lifetimes of excited states measured for $^{84,86}\text{Se}$ [18].

The present work focuses on the collectivity near the magic neutron number $N = 50$ and reports the extraction of $B(E2; 0_1^+ \rightarrow 2_1^+) = B(E2 \uparrow)$ values for $^{88,90}\text{Kr}$ ($N = 52, 54$)

and ^{86}Se ($N = 52$) with reduced error bars as compared to the literature and, for the first time, presents absolute measurements of the $B(E2)$ strengths to higher-lying 2^+ states in $^{88,90}\text{Kr}$. The results are discussed in the framework of large-scale shell-model calculations in the $\pi(fpg)\text{-}\nu(sdgh)$ shell relative to a ^{78}Ni core using an effective two-body interaction derived from the Idaho N^3LO nucleon-nucleon potential with a $V_{\text{low-}k}$ renormalization procedure. We show that this minimally tuned shell-model setup reproduces the observed $B(E2)$ strengths distribution rather well in the chosen model space, with the effective charges adjusted only to reproduce the known transition strength in semimagic ^{86}Kr .

II. EXPERIMENT

The measurements were performed at the National Superconducting Cyclotron Laboratory [19] at Michigan State University. The secondary beams of $^{88,90}\text{Kr}$ (67 and 68 MeV/nucleon) and ^{86}Se (79 MeV/nucleon) were produced from projectile fragmentation of a stable ^{96}Zr beam, which was accelerated by the K500 and K1200 coupled cyclotrons to 120 MeV/nucleon. The primary beam then impinged on a 364, 374, or 255 mg/cm² ^9Be production target for ^{88}Kr , ^{90}Kr , and ^{86}Se , respectively. An aluminum wedge degrader with an areal density of 200 mg/cm² located at the midacceptance position of the A1900 fragment separator [20] was used to purify the fragments of interest within the secondary beam cocktails.

A 246 mg/cm² ^{209}Bi foil used to induce projectile Coulomb excitation was located at the target position of the S800 spectrograph [21]. The event-by-event identification of the scattered projectiles and the trajectory reconstruction used to extract the scattering angles utilized the detection system of the spectrograph's focal plane, consisting of an ionization chamber, two xy -position-sensitive cathode-readout drift chambers, and a plastic timing scintillator that also served as

*Present address: National Superconducting Cyclotron Laboratory, Michigan State University, East Lansing, Michigan 48824, USA.

†Present address: TRIUMF, 4004 Wesbrook Mall, Vancouver, British Columbia, Canada V6T 2A3.

‡Present address: Diamond Light Source, Harwell Science and Innovation Campus, Didcot, Oxfordshire, OX11 0DE, United Kingdom.

§Present address: Department of Physics, University of Tokyo, Hongo, Bunkyo-ku, Tokyo 113-0033, Japan.

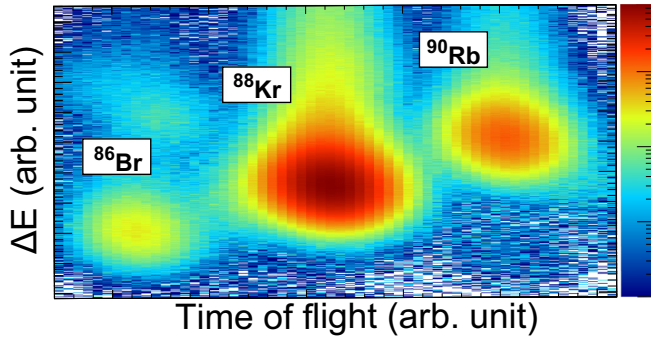


FIG. 1. Particle identification plot (energy loss versus Time of flight (arb. unit)) for $^{88}\text{Kr}^{35+}$. The beam components are cleanly separated and identifiable.

the particle trigger [22]. An example of the identification of the scattered ^{88}Kr projectiles emerging from the Bi target is shown in Fig. 1, where the energy loss measured with the S800 ionization chamber versus the ion's time of flight measured between two plastic scintillators is displayed. The ^{88}Kr nuclei can be clearly separated from the other constituents of the cocktail beam, i.e., ^{86}Br and ^{90}Rb . While the projectile beams delivered to the experiment were comprised of fully stripped ions, the scattered ions assumed a charge-state distribution after passage through the Bi target. For the Kr isotopes, the H-like charge state turned out to be the most intense and was centered in the S800 focal plane. For ^{86}Se , the fully stripped charge state was strongest and centered in the spectrograph. Typical S800 focal-plane rates were 1350 particles per second (pps) for $^{88}\text{Kr}^{35+}$, 350 pps for $^{90}\text{Kr}^{35+}$, and 20 pps for fully stripped ^{86}Se at incoming A1900 momentum acceptances of 0.5%, 1%, and 1%, respectively.

The Bi target was surrounded by the high-efficiency CsI(Na) scintillator array (CAESAR), an array of 192 closely packed scintillation crystals that cover almost 4π [23]. The high granularity of the array allowed for an event-by-event Doppler reconstruction of the γ rays emitted by the projectiles in flight. The angle of the γ -ray emission was deduced from the position of the CsI(Na) crystal that registered the highest energy deposition. The event-by-event Doppler-reconstructed γ -ray spectra detected in coincidence with $^{88,90}\text{Kr}$ and ^{86}Se are shown in Figs. 2(a)–2(c).

The energy-dependent photopeak efficiency of the setup was determined with ^{88}Y , ^{22}Na , ^{60}Co , and ^{137}Cs standard calibration sources. For the in-beam response of the array, the Lorentz boost of the emitted γ -ray distribution was taken into account via GEANT4 simulations. Scaling the GEANT4 simulated efficiency curve to the measured efficiencies and taking into account the uncertainties in the activity of each source resulted in an overall efficiency uncertainty of 5.4%.

III. METHODOLOGY AND RESULTS

Projectile Coulomb excitation is an experimental technique to quantify the low-lying quadrupole collectivity in short-lived nuclei. An ion beam of the rare isotope of interest is scattered off a stable high- Z target and is detected in coincidence with the deexcitation γ rays that tag and quantify the inelastic process [24–26].

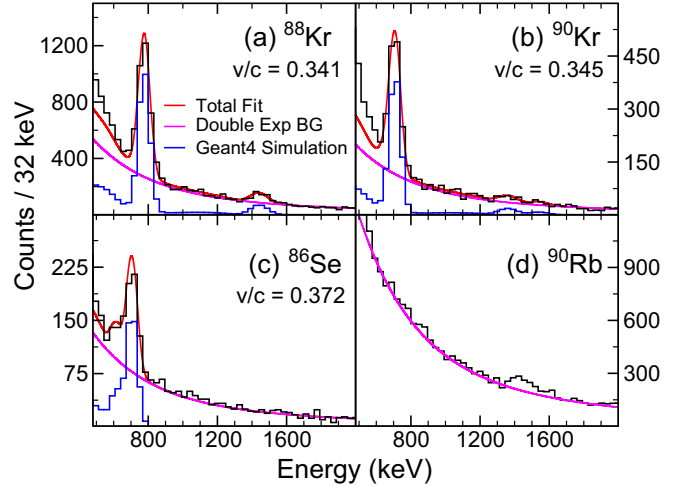


FIG. 2. (a)–(c) Doppler-corrected γ -ray spectra and fits to extract cross sections for the Coulomb excitation of states in each isotope. The GEANT4 fit template for each isotope is described in the text. (d) The spectrum of the beam contaminant ^{90}Rb was fit with a double exponential to model the prompt, beam-correlated background, using an exclusion region around the peaks near 1400 and 500 keV. The resulting double exponential fits the region containing all peaks of interest, which is from 600 keV to 1.7 MeV.

While beam energies below the Coulomb barrier prevent nuclear excitations, very peripheral collisions must be chosen in the regime of intermediate-energy Coulomb scattering to exclude nuclear contributions. This can be realized by restricting the data analysis to scattering events at very forward angles, corresponding to large minimum impact parameters, b_{\min} , in the collisions of projectile and target nuclei [25]. Angle-integrated cross sections for the Coulomb excitation are then deduced from the γ -ray intensities relative to the number of projectiles and the target thickness. Using the Alder-Winther model of relativistic Coulomb excitation [27], the electric quadrupole transition strength $B(E2 \uparrow)$ is then extracted from the cross sections.

Generally, impact parameters exceeding “touching sphere + 2 fm” have been proven sufficient to ensure the dominance of the electromagnetic interaction [26,28,29]. Through kinematics [27], the desired minimum impact parameter is translated into a maximum scattering angle to which the data analysis is then restricted. In the present work, a significant and asymmetric angle emittance of the incoming projectile beams was observed and has been taken into account in the determination of the maximum scattering angle as follows: For each isotope, the maximum scattering angle was determined using a minimum impact parameter corresponding to “touching sphere + 2 fm”. This led to maximum scattering angles, θ_{\max} , of 56, 53, and 45 mrad in the laboratory frame for ^{88}Kr , ^{90}Kr , and ^{86}Se , respectively. We then performed Monte Carlo simulations of the angular distribution in inelastic scattering by using the Alder-Winther formalism [27] to generate, for each scattering system, the input probability distribution over the range $0 \leq \theta \leq \theta_{\max}$ with the assumption that all events with angles beyond θ_{\max} are absorbed, corresponding to a sharp angle cutoff in a simplistic black-disk model. This

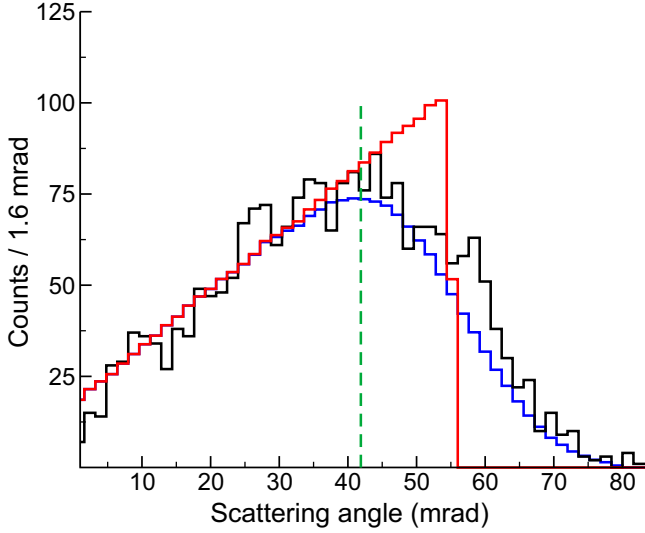


FIG. 3. Inelastic scattering distribution analysis for the example of ^{88}Kr . The red and blue lines are Monte Carlo simulations of the inelastic scattering process based on an input probability distribution from the Alder-Winther relativistic Coulomb excitation model, either with (blue) or without (red) the effects of angle emittances and straggling. The dashed green line shows the chosen, more restrictive, scattering-angle cut for the analysis of ^{88}Kr .

is shown in Fig. 3 for zero emittance (red line) and using the experimental beam emittance and the angular straggling deduced in comparison to LISE [30] from at most elastically scattered projectiles passing through the target (blue curve). As can be seen, close to the maximum-scattering-angle cutoff, one loses a fraction of the counts, corresponding to the difference between the red and blue curves.

We compare the results of the aforementioned simulation to our measured inelastic scattering distribution (black histogram), which is restricted to events in which only a $2_1^+ \rightarrow 0_1^+$ transition is observed. This measured scattering-angle distribution is overlaid and shows good agreement with the simulation that includes the realistic angle emittances and effects of straggling. To avoid this potential underestimation of counts and consequently of the angle-integrated cross section and the resulting $B(E2)$ value, a conservative maximum-scattering-angle cut, indicated by the dashed green line, was employed. Using this approach, more restrictive maximum-scattering-angle cuts of 42 mrad, 35 mrad, and 30 mrad in the laboratory frame were chosen for ^{88}Kr , ^{90}Kr , and ^{86}Se , respectively. We note that a similar analysis was performed in Ref. [31], where we could show that, away from the maximum scattering angle that corresponds to impact parameters where flux is removed from the (in)elastic channel, the effect of angle emittance and straggling is rather minor due to an approximate balance of events that scatter into and out of the angle cut applied to the data.

At intermediate and relativistic beam energies, multistep excitations are heavily suppressed. In even-even nuclei, this typically leads to the selective excitation of collective 2^+ states that are connected to the ground state by a sufficiently large branch. While most of the time only the first 2^+ state is

TABLE I. Measured cross sections, σ , and transition strengths, $B(E2)$, for all isotopes studied in this work, as well as transition strengths from the shell-model calculation described in Sec. IV are shown. The uncertainty includes both statistical uncertainties and systematic contributions from varying the background model, as well as a 5.4% uncertainty from the efficiency determination.

^AZ	J_i	J_f	σ (mb)	$B(E2; J_i \rightarrow J_f)$ ($e^2 \text{fm}^4$)	
				Measured	Shell model
^{88}Kr	0_1^+	2_1^+	210(30)	1310(190)	1450
	0_1^+	2_2^+	14(3)	90(20)	80
	2_2^+	2_1^+		$\leq 2010(450)$	440
	0_1^+	2_3^+	50(8)	320(50)	450
	2_3^+	2_1^+		$\leq 71^a$	69
	0_1^+	(2_4^+)	11(3)	70(20)	170
^{90}Kr	0_1^+	2_1^+	180(30)	1500(230)	1740
	0_1^+	2_2^+	40(10)	330(90)	580
	2_2^+	2_1^+		360(110)	280
	0_1^+	(2_3^+)	17(13)	150(110)	230
^{86}Se	0_1^+	2_1^+	230(30)	2110(320) ^b	1910
	0_1^+	2_2^+			150
	0_1^+	2_3^+			340

^aThe corresponding $B(M1; 2_3^+ \rightarrow 2_1^+) = 0.46(8)\mu_N^2$ strength was extracted using the multipole mixing ratio from Ref. [32] and compares well to our shell-model prediction of $0.51\mu_N^2$ obtained with standard orbital and spin nucleon g factors.

^bSee Sec. III C for discussion of possible unobserved feeding contributions.

observed, we report here the Coulomb excitation of higher-lying 2^+ states in $^{88,90}\text{Kr}$ as well. The angle-integrated Coulomb excitation cross sections for each state are determined from the γ -ray intensities of the deexciting transitions relative to the number of projectiles and number density of the target. This leads to several complications as compared to the typical intermediate-energy Coulomb excitation analysis where only the first excited state is observed. For the 2_1^+ state, feeding through $2_n^+ \rightarrow 2_1^+$ transitions has to be subtracted and, for the 2_n^+ states, branching ratios for the decays to the ground state and (typically) the 2_1^+ state have to be taken into account. Given CAESAR's modest in-beam γ -ray energy resolution of about 10% at 1 MeV, the fits that determine peak areas from complex spectra become important. Figure 2 shows in addition to the measured histograms also the results from GEANT4 simulations on top of background modeled by a double exponential based on the ^{90}Rb spectrum shown in Fig. 2(d). In the following, we discuss isotope by isotope the level schemes and assumptions that entered the determination of the Coulomb excitation cross sections. All results, including the measured cross section and extracted transition strength, are summarized in Table I.

A. ^{88}Kr

The primary fit template for ^{88}Kr included two peaks: the 775 keV transition from the 2_1^+ state to the ground state, and the 1440 keV transition from the 2_3^+ state at 2216 keV [see Fig. 2(a)]. However, we were able to identify two more feeding

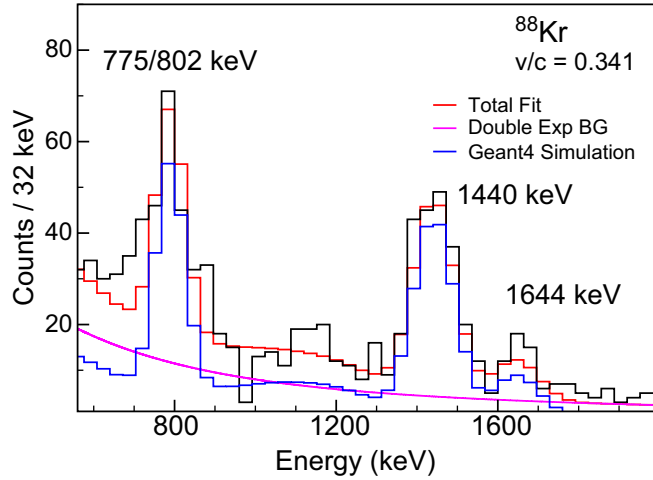


FIG. 4. Fit to extract feeding transitions in ^{88}Kr spectrum. The spectrum contains γ rays in coincidence with the 775 keV–802 keV doublet and there is a multiplicity-2 condition applied as explained in the text.

transitions, at 802 and 1644 keV, in a spectrum in coincidence with the 775 keV line as shown in Fig. 4.

The relevant level scheme of ^{88}Kr comprised of these transitions is shown in Fig. 5. All of these levels have been reported before in the literature [33].

Shown in Fig. 4 is the spectrum of γ rays in coincidence with the 775 keV transition, with a “multiplicity-2” condition applied; i.e., exactly two of the 192 CAESAR detectors registered an event within a prompt time gate. The multiplicity condition allows us to selectively reduce the beam correlated background, which is the primary source of background in our spectrum. Without applying this multiplicity condition on the coincidence matrix, we would not be able to separate the peak structures corresponding to weaker transitions from the background. Adding events with higher γ -ray multiplicity only added background to the coincidence matrix. In this coincidence matrix, we observed the 775 keV–802 keV coincidence, expected to originate from the 2_2^+ state at 1577 keV, and a 775 keV–1644 keV cascade, which would depopulate a state at 2419 keV. A level at this energy is known and tentatively assigned as the (3_1^-) state in the literature. We did not observe these two transitions in our γ singles spectrum shown in Fig. 2(a) due to the modest energy resolution of CAESAR in the case of the 802 keV transition and due to statistics for the 1644 keV transition.

With the $2_2^+ \rightarrow 2_1^+$ transition observed, one expects the $2_2^+ \rightarrow 0_1^+$ transition at a 26.34(24)% branching ratio [33]. Although this line is not visible in Fig. 2(a) since it is below the sensitivity limit of the spectrum, we could use the known branching ratio quoted above to determine the cross section $\sigma(0_1^+ \rightarrow 2_2^+)$ from the intensity of the $2_2^+ \rightarrow 2_1^+$ transition. The efficiency-corrected intensities of the 802 keV and 1644.3 keV transitions were extracted from the fit in Fig. 4. Because the 802 keV and the 775 keV transitions form a doublet within our resolution, both were included in this fit with the constraint that each would occur with equal intensity, as every 802 keV transition in multiplicity 2 is necessarily in coincidence with a 775 keV transition. The intensity of the

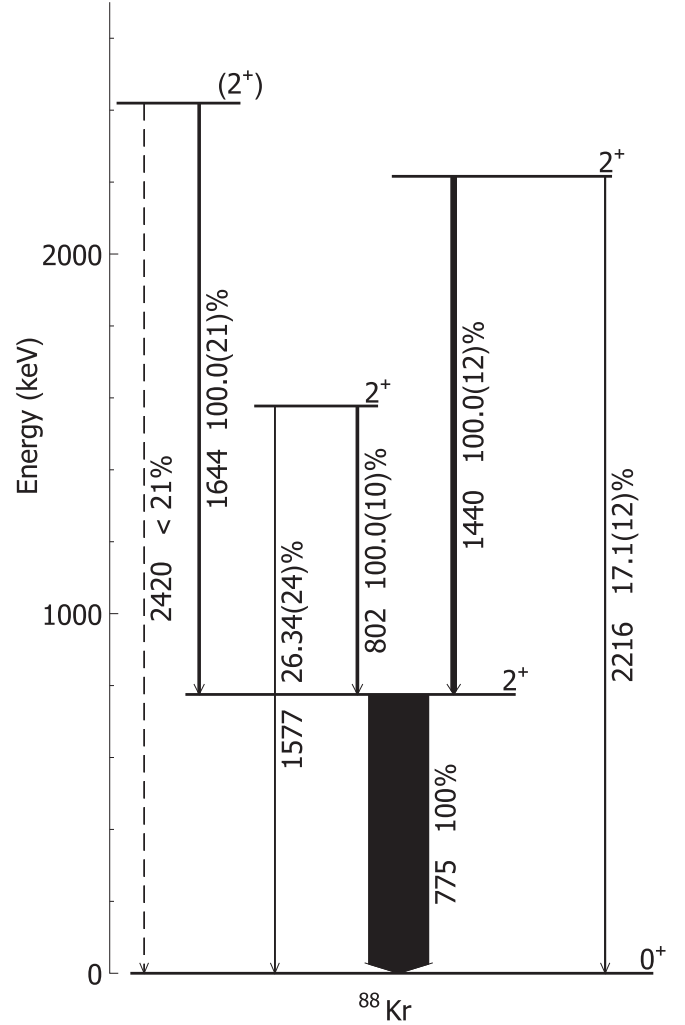


FIG. 5. Level scheme observed in this experiment for ^{88}Kr . The branching ratios are taken from Ref. [33]; the upper limit for the transition marked as a dashed line is based on the present work.

802 and 1644 keV transitions, along with the intensity of the 1440.5 keV transition from the direct fit shown in Fig. 2(a), were subtracted from the measured intensity of the 775 keV line. For this, the intensity of the 802 keV transition had to be accounted for twice, as it is included in the peak area of the 775 keV transition and it is indistinguishable in the fit of Fig. 2(a). The ratio of the intensities of the feeding transitions to the total measured 775 keV intensity was determined to be 25(4)%.

The measured cross sections and extracted transition strengths for ^{88}Kr are summarized in the top part of Table I. We note that $B(E2; 0_1^+ \rightarrow 2_1^+) = 900(90) e^2 \text{ fm}^4$ attributed to a subbarrier Coulomb excitation measurement is reported in conference proceedings [34] and a thesis [35]. Our result quoted in Table I exceeds this value by about 2σ .

Using the $B(E2; 0_1^+ \rightarrow 2_2^+)$ value determined here for the first time and the known branching ratio, we could extract the transition strength to the 2_1^+ state as $B(E2; 2_2^+ \rightarrow 2_1^+) = \frac{\delta^2}{1+\delta^2} 2010(450) e^2 \text{ fm}^4$, where δ is the unknown $E2/M1$ multipole mixing ratio. Table I quotes $2010(450) e^2 \text{ fm}^4$ as an upper limit for the $B(E2)$ strength.

For the 2_3^+ state, only the strong $2_3^+ \rightarrow 2_1^+$ branch was observed. The Coulomb excitation cross section, $\sigma(0_1^+ \rightarrow 2_3^+)$, was determined using the known branching ratio of 17.1(12)% [33] relative to the observed $2_3^+ \rightarrow 2_1^+$ transition. Our absolute measurement of $B(E2; 0_1^+ \rightarrow 2_3^+) = 320(50) e^2 \text{ fm}^4$ is consistent with the rather uncertain, previous measurement of $B(E2; 0_1^+ \rightarrow 2_3^+) = 400(200) e^2 \text{ fm}^4$ [32] from relativistic Coulomb excitation, which is quoted in Ref. [32] relative to the excitation of the first 2^+ state using the earlier-mentioned result published solely in proceedings [34]. Using the $E2/M1$ multipole mixing ratio of $\delta = 0.08_{-0.05}^{+0.09}$ from Ref. [32] and the known branching ratio, we deduce $B(M1; 2_3^+ \rightarrow 2_1^+) = 0.46(8) \mu_N^2$ and $B(E2; 2_3^+ \rightarrow 2_1^+) \leq 71 e^2 \text{ fm}^4$.

If the 2419 keV level that we observe was indeed a 3^- state, the intensity of the $(3^-) \rightarrow 2_1^+$ transition would require an unphysically large excitation strength of $B(E3; 0_1^+ \rightarrow (3^-)) > 204\,600 e^3 \text{ fm}^6$, corresponding to $B(E3 \downarrow) > 63 \text{ W.u.}$ for the deexcitation. This prompted us to tentatively assign $J^\pi = (2^+)$ for this state instead. This level has no previously reported ground-state transition and we do not observe this transition either, but we have determined an upper limit on the branching ratio of 21% based on our experimental sensitivity at this energy in the spectrum. In the calculation of the cross section and the $B(E2; 0_1^+ \rightarrow (2^+))$ value reported in Table I, a branching ratio of 10.5(105)%—exhausting our upper limit—was used.

Breaking down the error budget of the quoted transition strengths, in addition to the statistical and efficiency uncertainty, uncertainties for each extracted peak intensity were determined by systematically varying the fit template and background model and determining the effect on the extracted peak area. We determined this systematic uncertainty for the 775, 802, 1440, and 1644 keV transitions to be 8%, 7.7%, 12%, and 9.1%, respectively. The final quoted uncertainty for the 775 keV transition also includes the error propagated through the feeding subtraction.

B. ^{90}Kr

The fit template for the ^{90}Kr spectrum shown in Fig. 2(b) included the four transitions shown in Fig. 6 by the solid arrows. The 655 keV $2_2^+ \rightarrow 2_1^+$ transition was included although it forms a doublet with the 707 keV $2_1^+ \rightarrow 0_1^+$ transition by constraining its intensity through the known branching ratio of 68(4)%.

All transitions have been reported before in the literature, at precise energies of 707.05(6), 655.17(6), 1362.32(10), and 1542.20(13) keV [33]. Only the ground-state transition of the level at 2249 keV, which must exist for us to observe the excitation of this state, has not been reported so far.

To determine the $\sigma(0_1^+ \rightarrow 2_1^+)$ cross section, the intensities attributed to the $2_2^+ \rightarrow 2_1^+$ and $(2^+) \rightarrow 2_1^+$ feeders, amounting to a total of 11(5)% relative to the final intensity of the 707 keV peak, were subtracted. Our extracted $B(E2; 0_1^+ \rightarrow 2_1^+)$ value agrees with the only existing literature value [12] while being much more precise. With the known $E2/M1$ multipole mixing ratio $\delta = 0.507_{-0.022}^{+0.020}$ from Ref. [36], the $B(E2; 2_2^+ \rightarrow 2_1^+)$ strength was determined and is quoted in Table I in addition to the $B(E2; 0_1^+ \rightarrow 2_2^+)$ excitation strength.

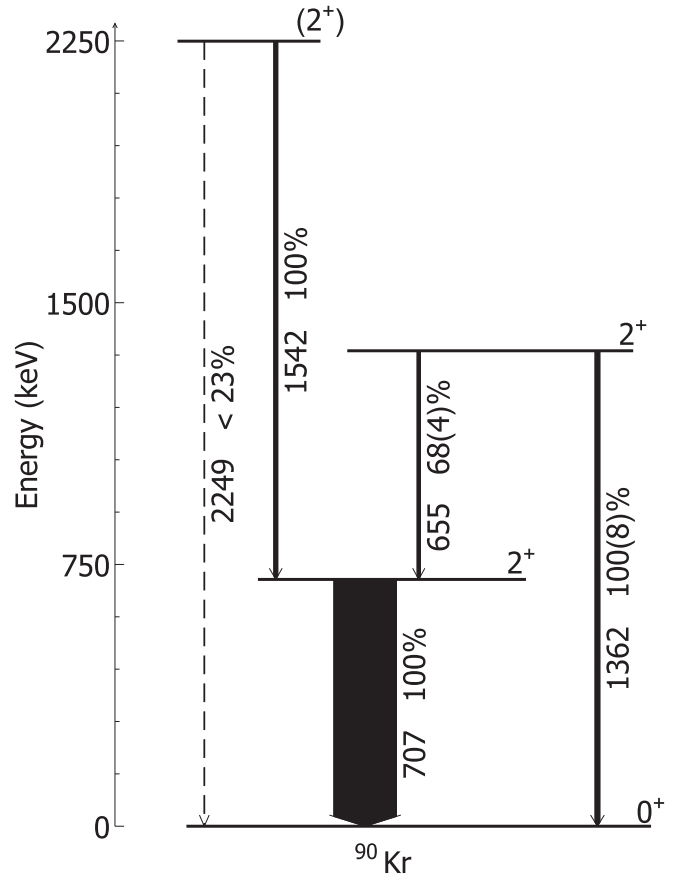


FIG. 6. Level scheme observed in this experiment for ^{90}Kr . The solid arrows indicate transitions that were observed in the present experiment. The branching ratios are taken from the literature [33]. The ground-state transition of the proposed higher-lying 2^+ state indicated by the dashed arrow is labeled with the upper limit for its branching as determined in our work from the sensitivity limit at this energy.

The level at 2249 keV has no J^π assignment in the literature. Similar to the case of the 2420 keV state in ^{88}Kr , we argue that this level is a higher-lying 2^+ state. For its branch to the ground state, we determine an upper limit of 23% from the sensitivity limit posed by our spectrum. For the calculation of the cross sections for the excitation of this state and the resulting $B(E2; 0_1^+ \rightarrow (2^+))$ value, the ground-state branching ratio was taken as 11.5(115)%, encompassing the upper limit. The results for ^{90}Kr are summarized in Table I.

For the final uncertainty on the transition strengths, uncertainties obtained by systematically varying our fit template and background model were added in quadrature to the statistical and the efficiency uncertainties. These systematic uncertainties were determined for the 655, 707, and 1542 keV transitions to be 30.4%, 10.4%, and 62%, respectively. The final quoted error for the 707 keV transition includes the contribution from feeding subtraction.

C. ^{86}Se

For ^{86}Se , only the transition from the 2_1^+ state to the ground state is clearly visible in the spectrum shown in

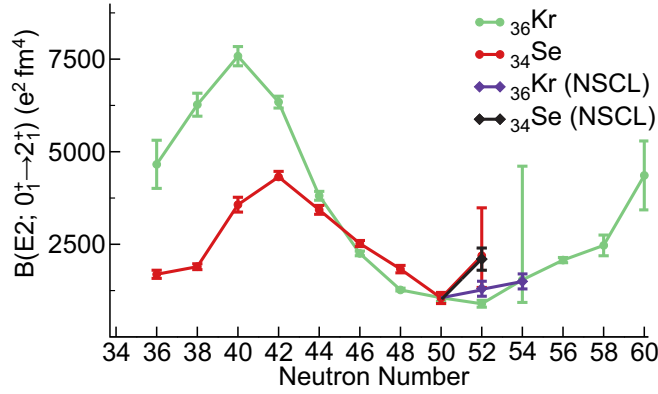


FIG. 7. Evolution of collectivity from $N = 36$ approaching $N = 60$ for the krypton and selenium isotopes including adopted values and the values measured here. The adopted values are taken from Ref. [38], except for the case for ^{86}Se [18].

Fig. 2(c). The shape of the corresponding peak at 704 keV, however, appears to have a low-energy shoulder, which may be explained by a peak at 613 keV. This transition energy had indeed been reported before [37] and, in that work, was tentatively suggested to directly feed the 2_1^+ state. However, if 613 and 704 keV were in immediate coincidence, this would lead to a second-excited, rather low-lying state of unknown nature. From our data, there is no evidence for a 704 keV–613 keV coincidence. Furthermore, this transition is considered unplaced in the evaluated data [33]. To account for this shoulder in the peak, two fitting strategies to extract the peak area of the 704 keV line were pursued: one that includes a peak at 613 keV and one that does not. Figure 2(c) shows the GEANT4 fit that does include a 613 keV line. Leaving out this peak worsens the χ^2 significantly but only increases the cross section and $B(E2)$ value from 227(34) mb and 2110(320) $e^2 \text{ fm}^4$ to 233(35) mb and 2170(330) $e^2 \text{ fm}^4$. In Table I, the first set of values is quoted.

$B(E2; 0_1^+ \rightarrow 2_1^+) = 2110(320) e^2 \text{ fm}^4$ determined in this work agrees, at much reduced uncertainty, with the literature value of $B(E2; 0_1^+ \rightarrow 2_1^+) = 2190_{-855}^{+1295} e^2 \text{ fm}^4$ that is based on an excited-state lifetime measurement [18].

The quoted uncertainty on the $B(E2)$ value includes a systematic uncertainty of 12.4% that was determined by allowing variations in the fit template and background model. This was added in quadrature to the statistical and efficiency uncertainties.

IV. DISCUSSION

The final results for the $B(E2; 0_1^+ \rightarrow 2_1^+)$ strength of $^{88,90}\text{Kr}$ and ^{86}Se are shown in Fig. 7. Our results for ^{90}Kr and ^{86}Se are consistent with previous measurements, with considerably reduced uncertainties. The ^{88}Kr measurement disagrees by more than 1σ with the previous measurement, but it is consistent with the expected evolution of collectivity relative to ^{86}Kr , namely, reduced $E2$ transition strength at the magic neutron number $N = 50$ relative to the even-even neighbors within the isotopic chain. With the reduced uncertainties of our results, the evolution of $B(E2)$ strength is now clearly consistent with the predicted smooth onset of collectivity [11,39].

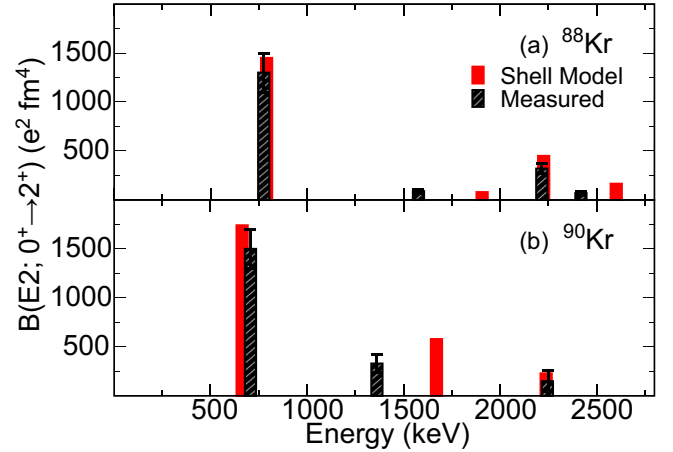


FIG. 8. Comparison of measured and calculated $B(E2)$ strengths for $^{88,90}\text{Kr}$ as a function of the energy of the 2_n^+ states.

The krypton isotopes exhibit significant excitation strength to several higher-lying 2^+ states, which had not been reported previously. To understand these $E2$ strength distributions, we compare to large-scale shell-model calculations. These were performed using the NUSHELLX@MSU [40] code with an effective two-body interaction derived from the Idaho $N^3\text{LO}$ nucleon-nucleon interaction [41]. The effective interaction was obtained using many-body perturbation theory to third order in the interaction following the recipe outlined in Refs. [31,42]. A ^{78}Ni core was used with single-particle energies taken from Ref. [43] or determined using Skyrme-Hartree-Fock calculations where missing. The model space includes the proton $1f_{5/2}$, $2p_{3/2}$, $2p_{1/2}$, and $1g_{9/2}$ orbitals and the neutron $1g_{7/2}$, $2d_{5/2}$, $2d_{3/2}$, $3s_{1/2}$, and $1h_{11/2}$ orbitals without subshell restrictions. The energy of the $g_{9/2}$ orbital was modified to reproduce the $9/2^+$ state in ^{87}Rb . The codes to derive the effective Hamiltonian, as well as the resulting effective interaction and single-particle energies used in the shell-model calculations, are publicly available [44].

To determine the effective charges that enter the calculation of $B(E2)$ values in the shell model, ^{86}Kr was computed within our shell-model setup and we adjusted the proton effective charge to $e_p = 1.68$ to reproduce the known $B(E2; 0_1^+ \rightarrow 2_1^+) = 1056(95) e^2 \text{ fm}^4$ value [45]. In a simple picture of isoscalar polarization charges, with $e_p = 1 + \delta_{\text{pol}}$ and $e_n = \delta_{\text{pol}}$, the neutron effective charge then amounts to $e_n = 0.68$. We note that these effective charges are comparable to those used in other recent calculations with a similar model space for this region [46].

The results of the shell-model calculation are shown in Fig. 8 and are tabulated in Table I. The shell-model calculation describes the measured distribution of $B(E2)$ strength rather well, which is particularly remarkable given the fact that our shell-model framework has very few parameters that are tuned (essentially the single-particle energies involved in the shell-model calculations). Also, the calculated $B(E2; 2_2^+ \rightarrow 2_1^+)$ value for ^{90}Kr agrees well with experiment (see Table I). For ^{88}Kr , the $B(E2; 2_2^+ \rightarrow 2_1^+)$ value quoted in the table is only an upper limit due to the unknown $E2/M1$ multipole mixing

ratio. Agreement between the measured and calculated transition strength would be reached with a multipole mixing ratio of $|\delta| = 0.53$, which is rather similar to the known $E2/M1$ mixing ratio of $\delta = 0.507^{+0.020}_{-0.022}$ [36] for the corresponding transition in neighboring ^{90}Kr .

Moschner *et al.* [32] discussed the 2_3^+ state of ^{88}Kr as a candidate for a proton-neutron mixed symmetry state [47], an isovector quadrupole excitation in the valence shell. The characteristic of such a state is a collective $M1$ transition to the first 2^+ level and a weakly collective $E2$ decay to the ground state. Using the literature branching ratio [33] and the $E2/M1$ multipole mixing ratio from Ref. [32], we deduce $B(M1; 2_3^+ \rightarrow 2_1^+) = 0.46(8)\mu_N^2$ and $B(E2; 2_3^+ \rightarrow 0_1^+) = 64(10) e^2 \text{fm}^4$ [or $2.8(4) \text{W.u.}$]. Both values are in agreement with the expectation for a $2_{m_s}^+$ state. The shell model predicts $B(M1; 2_3^+ \rightarrow 2_1^+) = 0.51\mu_N^2$ and $B(E2; 2_3^+ \rightarrow 0_1^+) = 90 e^2 \text{fm}^4$, close to the experimental values.

In ^{86}Se , the fragmentation of $E2$ strength to higher-lying 2^+ states is not observed. From the shell-model predictions provided in Table I, one may indeed have suspected that. To quantify this, we use the shell-model $B(E2; 0_1^+ \rightarrow 2_n^+)$ values to calculate how many counts should have been observed in our spectrum at the known decay energies and with the known branching ratios of the 1399 and 2208 keV states in ^{86}Se that are tentatively assigned as (2_2^+) and (2_3^+) [33]. For the decay of the 1399 keV state, 6(2) counts and 22(5) counts would be expected at 1399 keV $[(2_2^+) \rightarrow 0_1^+]$ and 695 keV $[(2_2^+) \rightarrow 2_1^+]$ in the singles spectrum. For the 2208 keV state, we would expect to observe 43(11) counts at 1504 keV $[(2_3^+) \rightarrow 2_1^+]$ and less than 2 counts at 2208 keV $[(2_3^+) \rightarrow 0_1^+]$. All of these transitions are below the sensitivity limit of the present measurement and, therefore, the data on ^{86}Se are consistent with the predicted magnitude of the $E2$ strength carried by higher-lying 2^+ states within the shell model. If we assume the feeder intensities determined using shell-model $B(E2)$ values and branching ratios, then the quoted $B(E2; 0_1^+ \rightarrow 2_1^+)$ would be reduced by 23%. As we do not observe these known transitions, this value can be considered an upper limit on the feeding from known states.

Table II shows the shell-model proton and neutron occupations for the states observed in the present work. Compared to another recent shell-model calculation for ^{90}Kr [36], for example, one observes very similar proton occupations, but for the neutrons, the occupations of $g_{7/2}$ and $h_{11/2}$ are essentially zero for us while they are 0.15 and 0.18, respectively, for the ground state of ^{90}Kr in Ref. [36].

TABLE II. Shell-model occupations of the proton and neutron orbitals for the observed levels in $^{88,90}\text{Kr}$ and ^{86}Se .

		Protons				Neutrons				
		$f_{5/2}$	$p_{3/2}$	$p_{1/2}$	$g_{9/2}$	$g_{7/2}$	$d_{5/2}$	$d_{3/2}$	$s_{1/2}$	$h_{11/2}$
^{88}Kr	0_1^+	4.29	2.74	0.62	0.35	0.01	1.88	0.04	0.06	0.02
	2_1^+	4.29	2.74	0.65	0.33	0.00	1.88	0.03	0.08	0.01
	2_2^+	4.21	2.84	0.72	0.23	0.00	1.83	0.03	0.12	0.01
	2_3^+	4.28	2.69	0.79	0.24	0.00	1.86	0.05	0.08	0.01
	2_4^+	4.60	2.64	0.55	0.21	0.01	1.84	0.04	0.09	0.02
^{90}Kr	0_1^+	3.96	2.96	0.79	0.29	0.01	3.68	0.16	0.13	0.03
	2_1^+	3.93	2.99	0.80	0.27	0.01	3.66	0.14	0.18	0.02
	2_2^+	3.85	2.80	1.15	0.20	0.01	3.57	0.19	0.21	0.02
	2_3^+	3.81	3.10	0.87	0.22	0.01	3.57	0.11	0.29	0.02
	2_4^+									
^{86}Se	0_1^+	3.50	1.84	0.41	0.24	0.01	1.80	0.06	0.12	0.01
	2_1^+	3.55	1.82	0.41	0.21	0.01	1.76	0.05	0.17	0.01

V. SUMMARY

The $B(E2; 0_1^+ \rightarrow 2_n^+)$ excitation strengths are reported for $^{88,90}\text{Kr}$ and ^{86}Se , with significantly reduced uncertainties as compared to previous measurements. Previously, the $B(E2; 0_1^+ \rightarrow 2_1^+)$ values for ^{90}Kr and ^{86}Se were the least precise in their respective isotopic chains. Furthermore, we observed a sizable fragmentation of the $B(E2)$ strength to higher-lying 2^+ states in $^{88,90}\text{Kr}$, in remarkable agreement with large-scale shell-model calculations that are based on a minimally tuned single-particle basis and an effective shell-model interaction based on modern nucleon-nucleon interactions from chiral effective field theory.

ACKNOWLEDGMENTS

This work was supported by the National Science Foundation (NSF) under Grant No. PHY-1102511, by the DOE National Nuclear Security Administration through the Nuclear Science and Security Consortium, under Award No. DE-NA0003180, and by the Department of Energy, Office of Nuclear Physics, under Grants No. DE-FG02-94ER40834 (Maryland) and No. DE-FG02-08ER41556 (MSU). M.H.-J. acknowledges NSF Grant No. PHY-1404159 (MSU). We are indebted to Diego A. Torres Galindo for generating the Skyrme-Hartree-Fock single-particle energies.

- [1] E. Cheifetz, R. C. Jared, S. G. Thompson, and J. B. Wilhelmy, *Phys. Rev. Lett.* **25**, 38 (1970).
- [2] H. Wollnik, F. Wohn, K. Wünsch, and G. Jung, *Nucl. Phys. A* **291**, 355 (1977).
- [3] F. Buchinger, E. B. Ramsay, E. Arnold, W. Neu, R. Neugart, K. Wendt, R. E. Silverans, P. Lievens, L. Vermeeren, D. Berdichevsky, R. Fleming, D. W. L. Sprung, and G. Ulm, *Phys. Rev. C* **41**, 2883 (1990).

- [4] E. Clément, M. Zielińska, A. Görgen, W. Korten, S. Péru, J. Libert, H. Goutte, S. Hilaire, B. Bastin, C. Bauer *et al.*, *Phys. Rev. Lett.* **116**, 022701 (2016).
- [5] E. Clément, M. Zielińska, S. Péru, H. Goutte, S. Hilaire, A. Görgen, W. Korten, D. T. Doherty, B. Bastin, C. Bauer *et al.*, *Phys. Rev. C* **94**, 054326 (2016).

- [6] J.-M. Régis, J. Jolie, N. Saed-Samii, N. Warr, M. Pfeiffer, A. Blanc, M. Jentschel, U. Köster, P. Mutti, T. Soldner *et al.*, *Phys. Rev. C* **95**, 054319 (2017).
- [7] P. Campbell, H. L. Thayer, J. Billowes, P. Dendooven, K. T. Flanagan, D. H. Forest, J. A. R. Griffith, J. Huikari, A. Jokinen, R. Moore *et al.*, *Phys. Rev. Lett.* **89**, 082501 (2002).
- [8] C. Kremer, S. Aslanidou, S. Bassauer, M. Hilcker, A. Krugmann, P. von Neumann-Cosel, T. Otsuka, N. Pietralla, V. Y. Ponomarev, N. Shimizu *et al.*, *Phys. Rev. Lett.* **117**, 172503 (2016).
- [9] T. Togashi, Y. Tsunoda, T. Otsuka, and N. Shimizu, *Phys. Rev. Lett.* **117**, 172502 (2016).
- [10] S. Naimi, G. Audi, D. Beck, K. Blaum, C. Böhm, C. Borgmann, M. Breitenfeldt, S. George, F. Herfurth, A. Herlert *et al.*, *Phys. Rev. Lett.* **105**, 032502 (2010).
- [11] M. Albers, N. Warr, K. Nomura, A. Blazhev, J. Jolie, D. Mücher, B. Bastin, C. Bauer, C. Bernards, L. Bettermann *et al.*, *Phys. Rev. Lett.* **108**, 062701 (2012).
- [12] J.-M. Régis, J. Jolie, N. Saed-Samii, N. Warr, M. Pfeiffer, A. Blanc, M. Jentschel, U. Köster, P. Mutti, T. Soldner *et al.*, *Phys. Rev. C* **90**, 067301 (2014).
- [13] J. Dudouet, A. Lemasson, G. Duchêne, M. Rejmund, E. Clément, C. Michelagnoli, F. Didierjean, A. Korichi, G. Maquart, O. Stezowski *et al.*, *Phys. Rev. Lett.* **118**, 162501 (2017).
- [14] T. Materna, W. Urban, K. Sieja, U. Köster, H. Faust, M. Czerwiński, T. Rząca-Urban, C. Bernards, C. Fransen, J. Jolie *et al.*, *Phys. Rev. C* **92**, 034305 (2015).
- [15] I. N. Gratchev, G. S. Simpson, G. Thiamova, M. Ramdhane, K. Sieja, A. Blanc, M. Jentschel, U. Köster, P. Mutti, T. Soldner *et al.*, *Phys. Rev. C* **95**, 051302 (2017).
- [16] S. Chen, P. Doornenbal, A. Obertelli, T. R. Rodríguez, G. Authalet, H. Baba, D. Calvet, F. Château, A. Corsi, A. Delbart *et al.*, *Phys. Rev. C* **95**, 041302 (2017).
- [17] A. Gade, T. Baugher, D. Bazin, B. A. Brown, C. M. Campbell, T. Glasmacher, G. F. Grinyer, M. Honma, S. McDaniel, R. Meharchand *et al.*, *Phys. Rev. C* **81**, 064326 (2010).
- [18] J. Litzinger, A. Blazhev, A. Dewald, F. Didierjean, G. Duchêne, C. Fransen, R. Lozeva, K. Sieja, D. Verney, G. de Angelis *et al.*, *Phys. Rev. C* **92**, 064322 (2015).
- [19] A. Gade and B. M. Sherrill, *Phys. Scr.* **91**, 053003 (2016).
- [20] D. J. Morrissey, B. M. Sherrill, M. Steiner, A. Stolz, and I. Wiedenhoever, *Nucl. Instrum. Methods Phys. Res., Sect. B* **204**, 90 (2003).
- [21] D. Bazin, J. Caggiano, B. Sherrill, J. Yurkon, and A. Zeller, *Nucl. Instrum. Methods Phys. Res., Sect. B* **204**, 629 (2003).
- [22] J. Yurkon, D. Bazin, W. Benenson, D. J. Morrissey, B. M. Sherrill, D. Swan, and R. Swanson, *Nucl. Instrum. Methods Phys. Res., Sect. A* **422**, 291 (1999).
- [23] D. Weisshaar, A. Gade, T. Glasmacher, G. F. Grinyer, D. Bazin, P. Adrich, T. Baugher, J. M. Cook, C. A. Diget, S. McDaniel *et al.*, *Nucl. Instrum. Methods Phys. Res., Sect. A* **624**, 615 (2010).
- [24] T. Motobayashi, Y. Ikeda, K. Ieki, M. Inoue, N. Iwasa, T. Kikuchi, M. Kurokawa, S. Moriya, S. Ogawa, H. Murakami, S. Shimoura, Y. Yanagisawa, T. Nakamura, Y. Watanabe, M. Ishihara, T. Teranishi, H. Okuno, and R. Casten, *Phys. Lett. B* **346**, 9 (1995).
- [25] T. Glasmacher, *Annu. Rev. Nucl. Part. Sci.* **48**, 1 (1998).
- [26] A. Gade and T. Glasmacher, *Prog. Part. Nucl. Phys.* **60**, 161 (2008).
- [27] A. Winther and K. Alder, *Nucl. Phys. A* **319**, 518 (1979).
- [28] J. M. Cook, T. Glasmacher, and A. Gade, *Phys. Rev. C* **73**, 024315 (2006).
- [29] F. Delaunay and F. M. Nunes, *J. Phys. G* **34**, 2207 (2007).
- [30] O. B. Tarasov and D. Bazin, *Nucl. Instrum. Methods Phys. Res., Sect. B* **376**, 185 (2016).
- [31] V. M. Bader, A. Gade, D. Weisshaar, B. A. Brown, T. Baugher, D. Bazin, J. S. Berryman, A. Ekström, M. Hjorth-Jensen, S. R. Stroberg *et al.*, *Phys. Rev. C* **88**, 051301 (2013).
- [32] K. Moschner, A. Blazhev, J. Jolie, N. Warr, P. Boutachkov, P. Bednarczyk, K. Sieja, A. Algora, F. Ameil, M. A. Bentley *et al.*, *Phys. Rev. C* **94**, 054323 (2016).
- [33] Evaluated Nuclear Structure Data File (ENSDF), <http://www.nndc.bnl.gov/ensdf>.
- [34] D. Mücher *et al.*, *AIP Conf. Proc.* **1090**, 587 (2009).
- [35] D. Mücher, Ph.D. thesis, Universität zu Köln, Köln, Germany, 2009 (unpublished).
- [36] T. Rząca-Urban, K. Sieja, W. Urban, M. Czerwiński, A. Blanc, M. Jentschel, P. Mutti, U. Köster, T. Soldner, G. de France, G. S. Simpson, and C. A. Ur, *Phys. Rev. C* **95**, 064302 (2017).
- [37] C. Mazzocchi, K. P. Rykaczewski, R. Grzywacz, P. Bączyk, C. R. Bingham, N. T. Brewer, C. J. Gross, C. Jost, M. Karny, A. Korgul *et al.*, *Phys. Rev. C* **92**, 054317 (2015).
- [38] B. Pritychenko, M. Birch, B. Singh, and M. Horoi, *At. Data Nucl. Data Tables* **107**, 1 (2016).
- [39] F. Flavigny, P. Doornenbal, A. Obertelli, J.-P. Delaroche, M. Girod, J. Libert, T. R. Rodríguez, G. Authalet, H. Baba, D. Calvet *et al.*, *Phys. Rev. Lett.* **118**, 242501 (2017).
- [40] B. A. Brown and W. D. M. Rae, *Nucl. Data Sheets* **120**, 115 (2014).
- [41] D. R. Entem and R. Machleidt, *Phys. Rev. C* **68**, 041001 (2003).
- [42] M. Hjorth-Jensen, T. Kuo, and E. Osnes, *Phys. Rep.* **261**, 125 (1995).
- [43] O. V. Bespalova, T. A. Ermakova, E. A. Romanovskii, T. I. Spasskaya, and A. A. Klimochkina, *Bull. Russ. Acad. Sci. Phys.* **73**, 816 (2009).
- [44] M. Hjorth-Jensen, Computational Environment for Nuclear Structure (CENS). All codes used to generate the effective interactions are available at <https://github.com/ManyBodyPhysics/CENS>. The specific effective interactions and single-particle energies are available from <https://github.com/ManyBodyPhysics/CENS/tree/master/FCI/parallel/pnCase/benchmarks/Mass78>.
- [45] T. J. Mertzimekis, N. Benczer-Koller, J. Holden, G. Jakob, G. Kumbartzki, K.-H. Speidel, R. Ernst, A. Macchiavelli, M. McMahan, L. Phair *et al.*, *Phys. Rev. C* **64**, 024314 (2001).
- [46] K. Sieja, T. R. Rodríguez, K. Kolos, and D. Verney, *Phys. Rev. C* **88**, 034327 (2013).
- [47] N. Pietralla, P. von Brentano, and A. Lisetskiy, *Prog. Part. Nucl. Phys.* **60**, 225 (2008).